SELF-CALIBRATION OF A 3D RANGE CAMERA

Derek D. Lichti

Department of Geomatics Engineering, Schulich School of Engineering, The University of Calgary, 2500 University Dr NW, Calgary AB T2N 1N4, Canada, - ddlichti@ucalgary.ca

Commission V, WG V/3

KEY WORDS: Range camera, calibration, modelling, error, performance analysis, bundle adjustment

ABSTRACT:

This paper proposes a new, integrated method for the self-calibration of 3D laser range cameras (LRCs) and corresponding systematic error models. Unlike other recently-proposed methods that consider independent sub-system calibration, this method allows simultaneous calibration of the camera-lens and rangefinder systems. The basis of the modelling is the collinearity and range observation equations augmented with systematic error correction terms that are estimated in a free-network, self-calibrating bundle adjustment. Several experiments designed to test the effectiveness of different combinations of systematic error model parameters on a SwissRanger SR-3000 LRC are described: a highly-redundant self-calibration network; an accuracy assessment test in which independently-surveyed target co-ordinates are compared with those from the LRC; and measurement of a planar surface. The former two tests reveal that an 11-parameter physical model is needed to correct all significant systematic errors. The latter experiment demonstrates the need for two additional empirical error terms for correcting residual rangefinder errors. Colour-dependent biases in the rangefinder measurements were found to cause the range observation residuals to be undesirably inflated.

1. INTRODUCTION

Laser range cameras (LRCs) or range imaging cameras can simultaneously capture a full 3D point cloud with an array sensor at video rates by time-of-flight rangefinding within a narrow field of view. They offer great potential for real-time measurement of static and, perhaps more importantly, dynamic scenes. Their principal advantage over laser scanners is the lack of a scanning mechanism and over digital cameras is that only one sensor is needed for 3D data capture. There are already numerous applications of this technology that include face detection (Hansen et al., 2007), mobile robot search and rescue (Ellekilde et al., 2007), gesture recognition for human-computer interaction (Holte et al., 2007; Breuer et al., 2007), manufacturing, automated vehicle guidance, guidance for the blind and wheelchair assistance (Bostelman et al., 2006). Others include video gaming, real-time foot mapping for podiatry, pedestrian sensing for automobile collision avoidance and person tracking for airport security.

The full metric potential of LRCs can not be realised, though, without a complete systematic error model and an associated calibration procedure to estimate all model coefficients. The recent research efforts of some have focused on the application of standard camera calibration procedures for the camera-lens system (Reulke, 2006; Santrac et al., 2006). Others have considered independent calibration of the camera-lens and rangefinder systems (Kahlmann et al., 2007; Lindner and Kolb, 2006) where the latter is calibrated using a combination of baseline and surface fitting methods. The challenge of a complete system calibration has been stated by Breuer et al., (2007): "Comprehensive calibration turned out to be very difficult". A new, integrated calibration approach that addresses this challenge is presented herein. Unlike the methods of others, the approach taken here is simultaneous calibration of both the rangefinder and the camera-lens systems.

This paper is structured as follows. First, the mathematical models are presented. This includes the observation equations, the systematic error models and the calibration solution method. Following a description of the LRC used, three experiments are described: one in which the LRC is calibrated and two in which the efficacy of the calibration is independently assessed. Results from these experiments are analysed in detail with particular attention paid to model efficacy, solution strength as measured by parameter correlation and the accuracy improvement resulting from the calibration.

2. MATHEMATICAL MODELS

2.1 Observation Equations

The basic observation equations logically stem from the fact that a LRC delivers radiometric intensity and 3D co-ordinates at each pixel location. Thus for any point i appearing in the focal plane of image j two collinearity equations

$$x_{ij} = x_{p_j} - c_j \frac{U_{ij}}{W_{ij}} + \Delta x \tag{1}$$

$$y_{ij} = y_{p_j} - c_j \frac{V_{ij}}{W_{ij}} + \Delta y \tag{2}$$

and one range equation

$$\rho_{ij} = \sqrt{\left(X_i - X_j^c\right)^2 + \left(Y_i - Y_j^c\right)^2 + \left(Z_i - Z_j^c\right)^2} + \Delta\rho \tag{3}$$

can be written, where

$$\begin{pmatrix} U \\ V \\ W \end{pmatrix}_{ij} = R_3(\kappa)R_2(\phi)R_1(\omega) \begin{pmatrix} X_i - X_j^c \\ Y_i - Y_j^c \\ Z_i - Z_j^c \end{pmatrix} \qquad (4)$$

and $(x, y, \rho)_{ij}$ are the observables; $(X, Y, Z)_i$ are the object-space co-ordinates of point i; the parameters $(X^c, Y^c, Z^c, \omega, \phi, \kappa)_j$ comprise the exterior orientation (EO) elements of image j; R_1, R_2, R_3 are the fundamental rotation matrices; $(x_p, y_p, c)_j$ are the interior orientation elements (IO) of image j; and $(\Delta x, \Delta y, \Delta \rho)$ represent the correction models for systematic errors in each observable.

2.2 Systematic Error Models

The camera-lens system error model used for LRC calibration is the standard model for digital cameras (e.g., Fraser, 1997),

$$\Delta x = \overline{x}\left(k_1 r^2 + k_2 r^4 + k_3 r^6\right) + p_1\left(r^2 + 2\overline{x}^2\right) + 2p_2\overline{x}\overline{y} \\ + a_1\overline{x} + a_2\overline{y} \qquad (5)$$

$$\Delta y = \overline{y}\left(k_1 r^2 + k_2 r^4 + k_3 r^6\right) + p_2\left(r^2 + 2\overline{y}^2\right) + 2p_1\overline{x}\overline{y} \qquad (6)$$

where (k_1, k_2, k_3) are the radial lens distortion coefficients; (p_1, p_2), are the decentring distortion terms; (a_1, a_2) are the electronic biases and

$$\overline{x} = x_{ij} - x_{p_j} \qquad (7)$$

$$\overline{y} = y_{ij} - y_{p_j} \qquad (8)$$

$$r^2 = \overline{x}^2 + \overline{y}^2 \qquad (9)$$

The rangefinder model comprises terms that have physical explanation (the d-terms and the first two e-terms) as well as empirical terms

$$\Delta\rho = d_0 + d_1\rho + \sum_{k=1}^{3}\left[d_{2k}\sin\left(\frac{2^k\pi}{U}\rho\right) + d_{2k+1}\cos\left(\frac{2^k\pi}{U}\rho\right)\right] \qquad (10)$$

$$+ e_1\overline{x} + e_2\overline{y} + e_3 r + e_4 r^2 + \sum_{m=2}^{3}\sum_{n=0}^{m} e_{3m+n-1}\overline{x}^{m-n}\overline{y}^n$$

where d_0 is the rangefinder offset; d_1 is the scale error; d_2 to d_7 are the cyclic error terms; U is the unit wavelength; e_1 and e_2 are the clock skew errors (Du et al., 2005); and e_3 to e_{11} represent empirical terms. In contrast to Lindner and Kolb (2006), who use B-splines to model the cyclic errors, the modelling approach chosen here is primarily driven by the known physical causes of these periodic effects (e.g., Rüeger, 1990).

Hereafter the IO shall be understood to comprise the principal point, principal distance plus this set of additional parameters (APs; Equations 5, 6 and 10). The IO shall be considered network-invariant for a given sensor.

2.3 Self-Calibration Solution and Spatial Distances

For the integrated self-calibration all model terms (EO, IO, and object points) are simultaneously estimated in a free-network adjustment with inner constraints imposed on the object points.

In addition, spatial distance observations between object points m and n

$$s_{mn} = \sqrt{\left(X_n - X_m\right)^2 + \left(Y_n - Y_m\right)^2 + \left(Z_n - Z_m\right)^2} \qquad (11)$$

are included to allow estimation of the scale error.

3. EXPERIMENT DESCRIPTION

3.1 Hardware

The subject of this study was the SwissRanger SR-3000 LRC system pictured in Figure 1. The principles of 3D range camera technology can be found in Lange and Seitz (2001), for example. The SR-3000 features a 176 pixel x 144 pixel array for which the pixel size and spacing are both 40 μm. The nominal principal distance of the lens is 8 mm. Several rangefinder system parameters such as the integration time and modulation frequency can be set by the user. For the experiments described herein, the former was set to the highest possible value of 51.2 ms so as to maximise the signal-to-noise ratio and the latter was 20 MHz, for which the corresponding maximum unambiguous range and, therefore, the unit length, is 7.5 m.

Figure 1. The SR-3000.

3.2 Target Field

The integrated calibration approach required special considerations in terms of both geometric network design and target design. A purpose-built, multi-resolution field of high-contrast (black on white) targets measuring 3.6 m x 2.0 m was constructed. An SR-3000 intensity image of the target field is shown in Figure 3. The targets were mounted on two planar surfaces separated by 0.8 m to provide depth relief. Several sizes of rectangular targets were used since the network comprised images captured at multiple ranges, a requirement for estimation of the rangefinder APs.

Several factors motivated this design. First, as the corners of the black rectangles constitute the targets, it was easy to measure spatial distances between targets. Second, no eccentricity correction was needed as is the case when circular targets are used (e.g., Ahn et al., 1999). Third, the materials were readily available. The disadvantage of this design stems from range biases that exist as a function of surface reflectivity (i.e. colour).

Since the target points lie at the boundary of two differently-coloured materials, the biases cause inflation of the range residuals, as will be demonstrated. Other researchers have, however, used similar black-and-white checkerboard patterns for their LRC calibration (Lindner and Kolb, 2006; Santrac et al., 2006).

3.3 Data Capture

For the calibration a network of 30 convergent images, 15 with κ=0° and 15 with κ=90°, was captured, as pictured in Figure 2. The images were captured about 1.0 m above the ground along two lines such that the convergence angle between them was approximately 80°. The minimum and maximum observed ranges were 1.1 m and 6.6 m, respectively. This range of distances is slightly smaller than that of Lindner and Kolb (2006) who performed their calibration between ranges of 0.75 m to 7.5 m.

Thirty-three spatial distances between various object points measured with a 1 m long, 0.5 mm graduated steel ruler were included in the network. The same target field was used for the accuracy assessment, but a set of 6 independent images were captured at different locations. Forty-nine object points distributed throughout the target field were surveyed with a total station to provide the basis for the accuracy assessment.
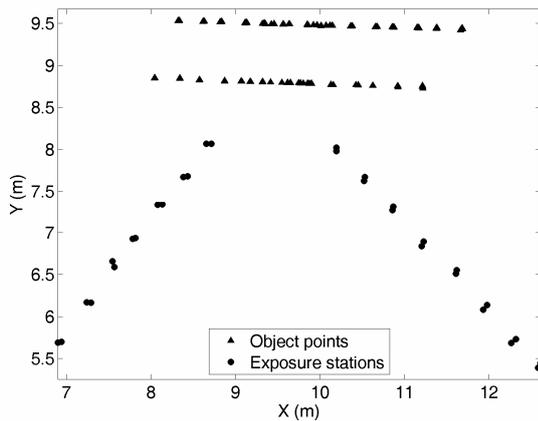

Figure 2. Calibration network.

3.4 Target Measurement

Measurement of the target corners, which constitute the object points, was performed as follows. First, edge detection was performed throughout the entire image using orthogonal first-derivative-of-Gaussian filters. For a given corner, the best-fit lines of the two intersecting edges were determined. This was done by fitting the following model to the edge magnitude image data

$$f(x, y) = Ae^{-Bu^2} + C + Gx + Hy \qquad (12)$$

where A is the amplitude of the Gaussian edge profile, C is the radiometric offset, G and H are the radiometric gradients, B is the damping coefficient and the line parameters D and θ are embedded in the function u:

$$u = x\cos\theta + y\sin\theta - D \qquad (13)$$

Once the parameters were estimated for each edge, the two lines were intersected to obtain the x, y co-ordinates of the target corner, as shown in Figure 3. The range at that location was then bi-linearly interpolated from those of the four neighbouring pixels.
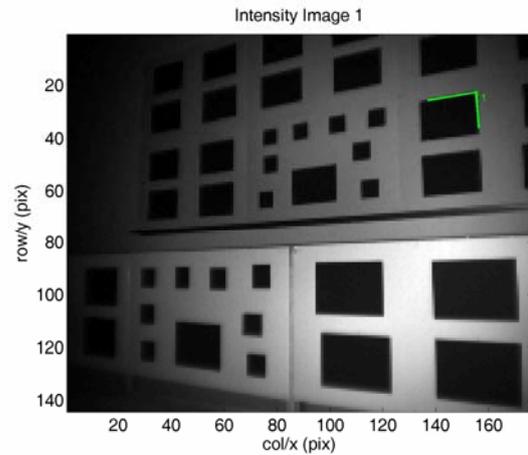

Figure 3. Target measurement by best fit line intersection.

4. SELF-CALIBRATION RESULTS AND ANALYSES

4.1 Self-Calibration Adjustment Cases

Four self-calibration adjustment cases were performed. These are summarised in Table 1. Case 1, for which no IO parameters were estimated, served as the basis for quantifying the improvements gained in the other three cases. Nominal values were used for the principal point, principal distance (8 mm) and rangefinder offset (300 mm). (The adjustment would not converge without the large nominal rangefinder offset.) In case 2 only these four "basic" IO parameters were estimated. In case 3 a complete physical model comprising only significant APs was estimated. Case 4 comprised the APs in case 3 plus two empirical terms identified through analyses of systematic patterns the estimated residuals. The degrees-of-freedom for free-network adjustment of case 4 was 6407.

Case	IO parameters estimated
1	None
2	"Basic" IO parameters: x_p, y_p, c, d_0
3	"Physical" IO parameters: x_p, y_p, c, k_1, d_0, d_4, d_5, d_6, d_7, e_1, e_2
4	Physical and empirical parameters: x_p, y_p, c, k_1, d_0, d_4, d_5, d_6, d_7, e_1, e_2, e_4, e_{11}

Table 1. Summary of the self-calibration cases

4.2 Model Efficacy

The improvements gained in each case can be assessed in terms of the RMS of residuals from all 7161 observations remaining after outlier removal by Baarda's data snooping. These figures are presented in Table 2 and show only minor improvement when the nominal IO parameters are estimated (case 2). Case 3 shows considerable improvement due to the large magnitude of the cyclic error components (maximum magnitude: 43 mm) and the clock-skew errors (maximum magnitude: 95 mm (range)/mm (image distance)). The latter correction equates to

334 mm at the edge of the image format. Another large correction of note is the 400 mm rangefinder offset. Little or no improvement is gained by adding the two empirical parameters in case 4 except in range, for which there is slight improvement.

Case	RMS			% improvement		
	x (μm)	y (μm)	ρ (mm)	x	y	ρ
1	11	8	171	-	-	-
2	10	7	160	9	12	6
3	6	5	50	45	38	71
4	7	5	46	36	38	73

Table 2. RMS of self-calibration residuals and % improvements

Focusing on case 3, the overall precision as measured by the RMS of residuals is quite good in both x and y at 6 μm and 5 μm, respectively, which represent 0.15 and 0.125 of the pixel size. This indicates that 1) the lens-system correction model was effective and 2) the image point measurement method of intersecting best-fit edge lines was very precise. At 50 mm, the range results are somewhat less impressive, though. This is most likely the due to the target design in which the observed distance was interpolated at the boundary between the white and black target components. Range biases were found between these two differently-coloured materials, which cased severe inflation of the range residuals. They can be seen in Figure 4 as the recessed rectangles in the range image. The magnitude of the bias can also be seen to vary with distance to the target. Note, however, that the gradual curving of the planar surfaces is expected in a range image.
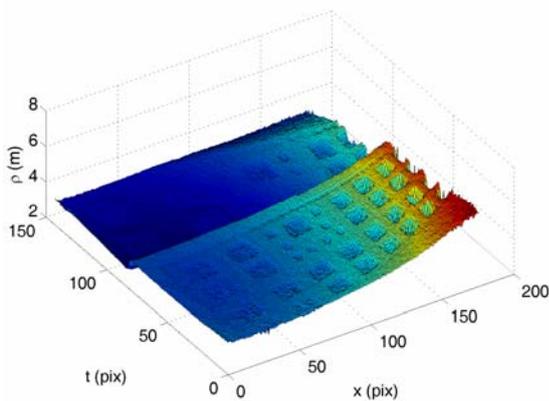

Figure 4. Range image showing biases due to the different target components as recessed rectangles.

This effect has also likely caused the estimated parameters, in particular the rangefinder offset, to be biased and, due to the high dispersion of observational errors, to be estimated with low precision (±2 mm for d_0 in case 3). The resulting high dispersion of the range residuals for case 3 can be seen in Figure 5 as a function of range. It is planned to use a circular target design for future calibrations.

4.3 Rangefinder Error Examples

Figure 6 shows the range residuals from case 3 excluding the cyclic error terms d_6 and d_7 to show the effect of this systematic error. Clearly a large-magnitude, periodic error exists. The

nominal wavelength is 1.875 m, one-quarter of the unit wavelength. Lindner and Kolb (2006) report a systematic deviation from the sinusoidal pattern of the cyclic errors at close range. No such effect was found in these data, though this may be due to the slightly-larger minimum range mentioned earlier.

Figure 7 shows the effect of excluding the e_2 clock-skew error term from the case 3 self-calibration solution. The result is a very strong linear trend in the range residuals as a function of the y image co-ordinate.
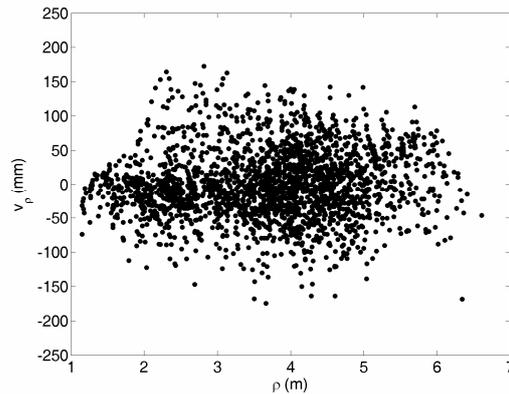

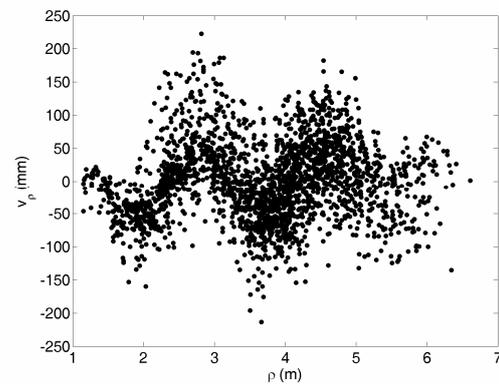Figure 5. Range residuals vs. range for case 3.

Figure 6. Range residuals vs. range for case 3 excluding the cyclic error parameters d_6 and d_7.
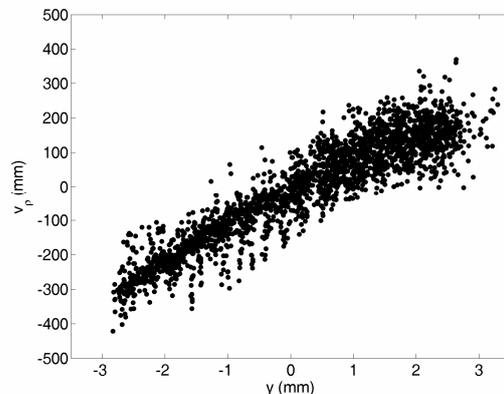

Figure 7. Range residuals vs. y for case 3 excluding the clock-skew parameter e_2.

4.4 Parameter Correlation

Considering again case 3, the largest correlation coefficients existed between the perspective centre co-ordinates (PCCs) and the principal distance (maximum magnitude: 0.83) and between the PCCs and the rangefinder offset (0.67). The maximum correlation magnitude between the rotation angles ω and ϕ and the principal point was quite favourable at 0.63, though it should be recalled that the IO model did not include decentring distortion terms, which were found to be insignificant. The only noteworthy correlation between the IO parameters was 0.71 between c and d_0. For the rest of the range APs the maximum correlation with any other parameter (EO or IO) was 0.20. Addition of the empirical terms in case 4 changed the situation, with maximum coefficients of 0.90 between e_2 and e_{11}, and 0.64 between d_0 and e_4. In both cases 3 and 4, though, all APs were statistically significant in terms of the ratio of the estimate to the standard deviation.

4.5 Scale Error Estimation

Addition of the scale error, d_1, to the case 3 adjustment did not significantly change the residual RMS measures. A high correlation of 0.86 existed with d_0 but, interestingly and encouragingly, the correlation with c was only 0.44. These could be reduced by increasing the depth variation in the target field. Though statistically significant, d_1 was excluded from the final AP models due to its lack of impact on the other performance measures. What this demonstrates is that the scale error parameter can be successfully estimated by including easily-measured spatial distance observations in the self-calibration adjustment, though it is conceded that a large number (33) were used in this experiment.

4.6 Lens Distortion Modelling Results

The estimated radial lens distortion profile, δr, of the SR-3000 is plotted in Figure 8. Though the amount of distortion is quite high, -205 μm at the maximum observed radial distance of 4.55 mm, this represents only about 5 pixels due to the 40 μm pixel size. The corresponding 1σ error envelope is not perceivable since the estimated standard deviation of k_1 was almost two orders of magnitude (76 times) smaller than k_1 itself. The higher order terms of the radial lens distortion model were found to be insignificant.
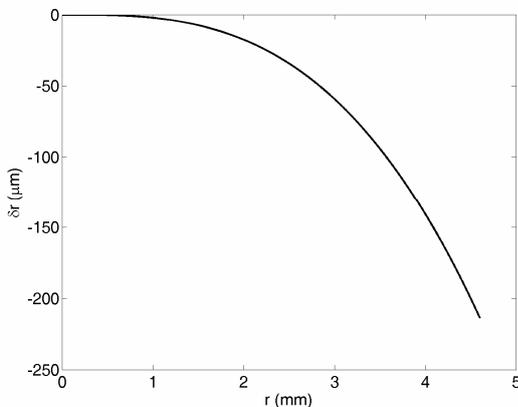

Figure 8. Estimated radial lens distortion profile.

5. INDEPENDENT ASSESSMENT

5.1 Accuracy Assessment

To assess the accuracy improvement gained by the different IO model cases, the object space co-ordinates of the surveyed points were compared with those determined from the LRC. A rigid body transformation of the LRC-determined co-ordinates onto the surveyed co-ordinates was required for each of the 6 independent images. The overall RMSs of co-ordinate differences calculated from the total available set of 188 points are given in Table 3. The case 2 IO set yields improvement in only one dimension (X) and the accuracy actually degrades slightly in Y and Z. Clearly there is considerable improvement realised by using the physical AP model (case 3). In case 4 there is more overall improvement in Z relative to case 3, but there also was a slight degradation in X, which may be due to over-parameterisation with the empirical terms.

	RMS			% improvement		
Case	**X (mm)**	**Y (mm)**	**Z (mm)**	**X**	**Y**	**Z**
1	47	57	70	-	-	-
2	42	63	74	11	-11	-7
3	31	14	43	34	75	37
4	35	15	36	27	74	48

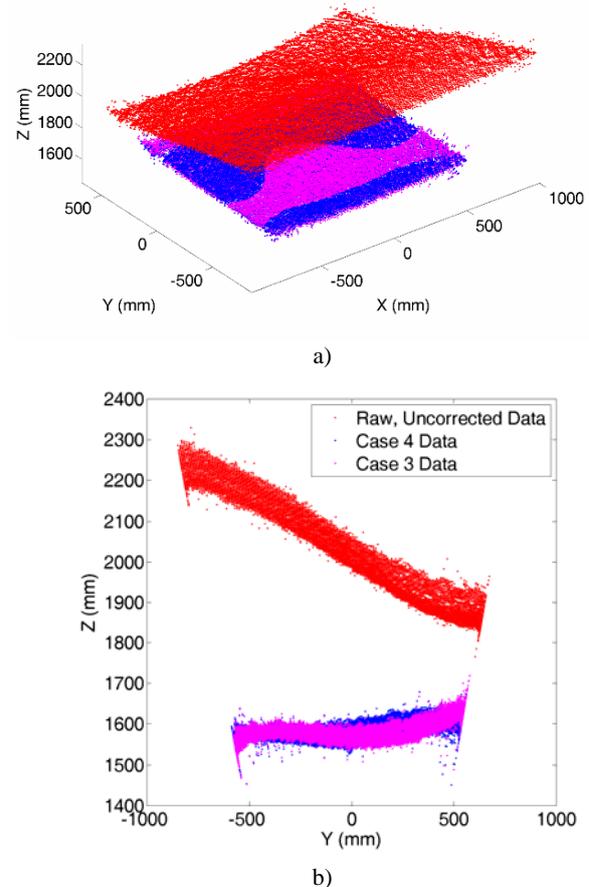Table 3. RMS of check point differences and % improvements.

a)

b)

Figure 9. Uncorrected and corrected planar target data. a) Isometric view, b) side view.

5.2 Planar Surface Correction

As a final indicator of the efficacy of the proposed models, a planar, matte white target was imaged with the same SR-3000 at normal incidence from a nominal distance of 1.5 m. The target filled the entire LRC field of view, so material reflectivity was constant throughout the image. Figure 9 shows two views of the raw, uncorrected point cloud and the data corrected with the case 3 and 4 models. Note the highly distorted shape of the raw data, the large (i.e. up to 800 mm) corrections in the Z co-ordinates (closely aligned to the range direction) and the residual un-flatness in the case 3 results. The latter is corrected by the two empirical terms included in the case 4 IO model.

6. CONCLUSIONS AND FURTHER WORK

An integrated method for LRC self-calibration and corresponding systematic error models have been proposed. Three particular IO models having 4, 11 and 13 parameters were examined in detail. In terms of model efficacy as measured by the RMS of self-calibration residuals, the 4-parameter, basic IO case was found to provide little improvement over the case of adjustment without any IO parameters. The other two models resulted in considerable improvement due to the large-magnitude range error correction terms that were estimated, but there was little difference between the two sets of results. The accuracy assessment test resulted in very similar outcomes. The example of planar surface correction demonstrated the benefit of the empirical terms that modelled residual un-flatness. The chosen target design provided good results in terms of the image co-ordinate measurement residuals, but less favourable results in terms of the range residuals due to surface reflectance dependent biases. A circular target design is currently being pursued to overcome this problem in order to improve the self-calibration results.

ACKNOWLEDGEMENTS

REFERENCES

Ahn, S. J., Warnecke, H.-J., and Kotowski, R., 1999. Systematic Geometric Image Measurement Errors of Circular Object Targets: Mathematical Formulation and Correction. *Photogrammetric Record*, 16 (93), pp. 485-502

Bostelman, R., Russo, P., Albus, J., Hong, T. and Madhavan, R., 2006. Applications of a 3D Range Camera Towards Healthcare Mobility Aids. *International Conference on Networking, Sensing and Control*, Ft. Lauderdale, FL, April 23-25, pp. 416-421.

Breuer, P., Eckes, C. and Müller, S., 2007. Hand gesture recognition with a novel IR time-of-flight range camera—a pilot study. In A. Gagalowicz and W. Philips (Eds.): *Lecture Notes in Computer Science*, Springer: Berlin, vol. 4418, pp. 247-260.

Du, H., Oggier, T., Lustenburger, F. and Charbon, E. 2005. A Virtual Keyboard Based on True-3D Optical Ranging, *Proceedings of the British Machine Vision Conference*, Oxford, Sep. 2005, 10 pp.

Ellekilde, L.-P., Huang, S., Miró, J.A. and Dissanayake, G., 2007. Dense 3D map construction for indoor search and rescue. *Journal of Field Robotics*, 24 (1/2), pp. 71-89.

Fraser, C.S., 1997. Digital camera self-calibration. *ISPRS Journal of Photogrammetry and Remote Sensing*, 52 (4), pp. 149-159.

Hansen, D.W., Larsen, R. and Lauze, F., 2007. Improving face detection with TOF cameras. In Proceedings of IEEE *International Symposium on Signals, Circuits & Systems*, Iasi, Romania, 12-13 July, 4 pp.

Holte, M.B., Moeslund, T.B. and Fihl, P., 2007. View invariant gesture recognition using the CSEM SwissRanger SR-2 camera. *Dynamic 3D Imaging Workshop*, Heidelberg, Germany, September 11, 7 pp.

Kahlmann, T., Remondino, F., Guillaume, S., 2007 Range imaging technology: new developments and applications for people identification and tracking. Proceedings of *Videometrics IX - SPIE-IS&T Electronic Imaging*, San Jose, CA, vol. 6491, 12 pp.

Lange, R. and Seitz, P., 2001. Solid-state time-of-flight range camera. *IEEE Transactions on Quantum Electronics,* 37 (3), pp. 390-397.

Lindner, M. and Kolb, A., 2006. Lateral and Depth Calibration of PMD-Distance Sensors, *Lecture Notes in Computer Science*, vol. 4292, Springer Berlin / Heidelberg, pp. 524-533.

Rüeger, J.M., 1990. *Electronic Distance Measurement: an Introduction*, third ed. Springer-Verlag, Heidelberg, Germany.

Santrac, N., Friedland, G., and Rojas, R., 2006. High Resolution Segmentation with a Time-of-Flight 3D-Camera using the Example of a Lecture Scene. Fachbereich mathematic und informatik, Freie Universität Berlin, B-06-09, 8 pp.